



COMMUNICATIONS PHYSICS

ARTICLE

DOI: 10.1038/s42005-018-0029-0

OPEN

A theory on skyrmion size

X.S. Wang^{1,2}, H.Y. Yuan³ & X.R. Wang^{1,4}

A magnetic skyrmion is a topological object consisting of a skyrmion core, an outer domain, and a wall that separates the skyrmion core from the outer domain. The skyrmion size and wall width are two fundamental quantities of a skyrmion that depend sensitively on material parameters such as exchange energy, magnetic anisotropy, Dzyaloshinskii-Moriya interaction, and magnetic field. However, quantitative understanding of the two quantities is still very poor. Here we present a general theory on skyrmion size and wall width. The two formulas we obtained agree almost perfectly with simulations and experiments for a wide range of parameters, including most of the existing materials that support skyrmions.

¹School of Electronic Science and Engineering and State Key Laboratory of Electronic Thin Film and Integrated Devices, University of Electronic Science and Technology of China, Chengdu 610054, China. ²Physics Department, The Hong Kong University of Science and Technology, Clear Water Bay, Kowloon 999077, Hong Kong. ³Department of Physics, Southern University of Science and Technology, Shenzhen 518055, China. ⁴HKUST Shenzhen Research Institute, Shenzhen 518057, China. Correspondence and requests for materials should be addressed to X.R.W. (email: phxwan@ust.hk)

Skyrmions, topological objects originally used to describe resonance states of baryons¹, were observed in magnetic systems that involve Dzyaloshinskii–Moriya interaction (DMI)^{2–13}. There are two types of topologically equivalent magnetic skyrmions. One is the Bloch skyrmions in systems with the bulk DMI^{3–7}. The other is the Néel skyrmions (also known as hedgehog skyrmions) in systems with interfacial DMI^{8–12}. Compared with traditional magnetic bubbles that are micrometer-size circular magnetic domains stabilized by dipole interactions^{14–17}, recently studied skyrmions have smaller size (1 nm ~ 100 nm) and better stability due to DMI. Also, the driven current density (order of 10^6 Am^{-2}) is much lower than that for magnetic domain walls (10^{12} Am^{-2})¹⁸. So the DMI-supported skyrmions are believed to be potential information carriers in future high-density data storage and information processing devices^{2–10,13,18–20}.

Although much knowledge about the DMI-supported magnetic skyrmions has been accumulated after intensive studies including skyrmion generation^{10,13,21,22} and manipulation^{18,23,24}, the dependence of skyrmion size (R) on material parameters such as exchange energy, magnetic anisotropy energy, and DMI strength is still poorly understood at a quantitative, or even qualitative level^{18,25–29}. Even worse, the physical pictures behind most previous studies are not clear. In this paper, we confirm by micro-magnetic simulations that the skyrmion profiles agree well with the 360° domain wall formula^{30,31} in a wide extent. By using this formula as an ansatz and minimizing the energy with respect to the skyrmion size R and the skyrmion wall width w as two independent quantities, we obtain the analytical expressions of R and w as functions of A , D , K , and B . Interestingly and in contrast to previous theories^{25,26,29}, R always decreases with A . In general, both R and w increase with D . These results agree perfectly with micromagnetic simulations and are consistent with experiments.

Results

Energy functional and approximate profile of isolated skyrmions. We consider an ultra-thin ferromagnetic film in xy plane with an exchange constant A , an interfacial DMI coefficient D , a perpendicular easy-axis anisotropy K , and a perpendicular magnetic field B . The total energy E of the system consists of the exchange energy E_{ex} , the DMI energy E_{DM} , the anisotropy energy E_{an} , and the Zeeman energy E_{Ze} ,

$$E = E_{\text{ex}} + E_{\text{DM}} + E_{\text{an}} + E_{\text{Ze}}, \quad (1)$$

where $E_{\text{ex}} = Ad \int |\nabla \mathbf{m}|^2 dS$, $E_{\text{DM}} = Dd \int [m_z \nabla \cdot \mathbf{m} - (\mathbf{m} \cdot \nabla) m_z] dS$, $E_{\text{an}} = Kd \int (1 - m_z^2) dS$, and $E_{\text{Ze}} = M_s B d \int (1 - m_z) dS$. \mathbf{m} is the unit vector of magnetization of a constant saturation magnetization M_s and the integration is over the whole film. The energy reference is chosen in such a way that the energy of single domain state of $m_z = 1$ is $E = 0$. We have assumed m is uniform in thickness direction. The demagnetization effect is included in E_{an} through the effective anisotropy $K = K_u - \mu_0 M_s^2 / 2$ corrected by the shape anisotropy, where K_u is the perpendicular magnetocrystalline anisotropy, which is a good approximation when the film thickness d is much smaller than the length w over which magnetization varies substantially. It is convenient to use polar coordinates so that a point \mathbf{r} in the plane is denoted by r and ϕ . Magnetization at \mathbf{r} is described by polar and azimuthal angles $\Theta(r, \phi)$ and $\Phi(r, \phi)$ so that $\mathbf{m} = (\sin \Theta \cos \Phi, \sin \Theta \sin \Phi, \cos \Theta)$. A skyrmion centered at $r = 0$ can be described¹⁹ by,

$$\Theta = \Theta(r), \quad \Phi = \nu \phi + \gamma, \quad (2)$$

with boundary conditions of $\Theta(0) = 0(\pi)$ and $\Theta(\infty) = \pi(0)$. ν is the vorticity ($\nu = 1$ for a skyrmion and $\nu = -1$ for an antiskyrmion), and

γ is a constant classifying type of skyrmions ($\gamma = 0$ or π for Néel skyrmions and $\gamma = \pm \pi/2$ for Bloch skyrmions). Similar to the magnetic bubbles^{14,16,17} that refer normally to local metastable structures from dipole interactions, a skyrmion consists of a skyrmion core, an outer domain, and a wall separating the core and the outer domain. We define the skyrmion size R as the radius of the $m_z = 0$ contour. The wall width w is another fundamental skyrmion quantity often ignored or not treated properly in previous studies^{25–28}. One can also define the skyrmion polarity as $p = [m_z(r = \infty) - m_z(r = 0)]/2$ so that $p = 1$ (-1) corresponds to spins in the core and outer domain pointing respectively to the $-z(+z)$ and $+z(-z)$ directions.

In terms of Θ , four energy terms for $\nu = 1$ are

$$E_{\text{ex}} = 2\pi Ad \int_0^\infty \left[\left(\frac{d\Theta}{dr} \right)^2 + \frac{\sin^2 \Theta}{r^2} \right] r dr, \quad (3)$$

$$E_{\text{DM}} = 2\pi Dd \cos \gamma \int_0^\infty \left(\frac{d\Theta}{dr} + \frac{\sin 2\Theta}{2r} \right) r dr, \quad (4)$$

$$E_{\text{an}} = 2\pi Kd \int_0^\infty \sin^2 \Theta r dr, \quad (5)$$

$$E_{\text{Ze}} = 2\pi M_s B d \int_0^\infty (1 - \cos \Theta) r dr. \quad (6)$$

For a skyrmion of $p = 1$ as shown in Fig. 1a, $\int_0^\infty \frac{d\Theta}{dr} r dr < 0$, because Θ decreases monotonically from $\Theta(0) = \pi$ to $\Theta(\infty) = 0$. $\int_0^\infty \frac{\sin 2\Theta}{2r} r dr = \int_0^\infty \sin \Theta \cos \Theta dr$ is small because $\sin \Theta \cos \Theta = 0$ far from the skyrmion wall and $\sin \Theta \cos \Theta$ changes its sign from negative near the skyrmion core to positive near the outer domain. Thus, to lower the total energy, one needs $\gamma = 0(\pi)$ for $D > 0$ (< 0). This corresponds to a Néel skyrmion. Along a radial direction, the magnetization profile looks like a 360° Néel domain wall as illustrated in Fig. 1b. This leads us to model a skyrmion profile by a 360° domain wall originally proposed by Braun³¹ (see Supplementary Note 1),

$$\Theta_{\text{dw}}(r) = 2 \arctan \left[\frac{\sinh(R/w)}{\sinh(r/w)} \right]. \quad (7)$$

It is worth mentioning that 360° domain wall profile has already been used to describe the skyrmion profile obtained in experiments^{30,32}.

To test how good ansatz (7) is for a skyrmion, we use MuMax3³³ to simulate various magnetic stable states (see Methods). $A = 15 \text{ pJm}^{-1}$, $M_s = 580 \text{ kAm}^{-1}$, and perpendicular easy-axis anisotropy $K_u = 0.8 \text{ MJm}^{-320}$ are used to mimic Co layer in Pt/Co/MgO system. The initial state is $m_z = 1$ for $r > 10 \text{ nm}$ and $m_z = -1$ for $r \leq 10 \text{ nm}$. The final stable state depends on the values of D and B . The lower left inset of Fig. 1 is three typical stable states. Figure 1c is a skyrmion for $D = 3.7 \text{ mJm}^{-2}$ and $B = 0$. Figure 1d is a single-domain state of $m_z = 1$ (or $m_z = -1$) for $D = 0$ and $B = 0$. Figure 1e is a stripe domains state for $D = 5 \text{ mJm}^{-2}$ and $B = 0$. Figure 1b shows the spatial distribution of m_z of the skyrmion in Fig. 1c along three radial directions, $\phi = 0$ (crosses), 45° (triangles), and 90° (circles). All three sets of data are on the same smooth curve, showing m_z is a function of r , but not ϕ . The curve can fit perfectly to Eq. (7) with $R = 25.77 \text{ nm}$, $w = 4.94 \text{ nm}$. We plotted also $\Phi(\phi)$ at randomly picked spins from the simulated skyrmion. All numerical data (red circles) are perfectly on $\Phi = \phi$. These results not only confirm the validity of Eq. (2), but also suggest that $m_z(r) \equiv \cos[\Theta_{\text{dw}}(r)]$ follows the 360° DW profile (7), although it is

not exact that can be easily verified by substituting Eq. (7) into the nonlinear partial differential equations for skyrmions²⁹.

Skyrmion size. The energy of a skyrmion can then be obtained from Eq. (3) by using the 360° domain wall profile $\Theta_{\text{dw}}(r)$. Substituting $\Theta_{\text{dw}}(r)$ into Eqs. (1) and (3), the total energy is, in general, a function of R and w [instead of a functional of $\Theta(r)$ and $\Phi(\phi)$] as

$$E(R, w) = 4\pi d \left\{ A \left[f_1\left(\frac{R}{w}\right) + f_2\left(\frac{R}{w}\right) \right] + Dw \left[f_3\left(\frac{R}{w}\right) + f_4\left(\frac{R}{w}\right) \right] + Kw^2 f_5\left(\frac{R}{w}\right) + \mu_0 M_s B w^2 f_6\left(\frac{R}{w}\right) \right\}, \quad (8)$$

where $f_i(x)$ ($i = 1 \sim 6$) are non-elementary functions defined in Methods. The skyrmion size and wall width R and w are the values that

minimize $E(R, w)$. In ref. 25, w was assumed to be a fixed value such as $w = \sqrt{A/K}$ that eventually leads to a wrong skyrmion size. Figure 2 are D - (a), A - (b), K - (c), and B - (d) dependences of the skyrmion size R (left y axis) and the skyrmion wall width w (right y axis), with other parameters fixed to the values for Co mentioned earlier. The symbols are the micromagnetic simulation data [R is the size of $m_z = 0$ contour and w is the fit of the skyrmion profile to $\Theta_{\text{dw}}(r)$]. The sample size used in the simulations is large enough to avoid the boundary effects (see Supplementary Fig. 1). Solid lines are numerical results from Eq. (8). The simulation results agree almost perfectly (except slight deviation in the D -dependence of w for smaller D) with our analytic results of Eq. (8). Both micromagnetic simulations and analytical results clearly show that the skyrmion can exist for $D < 3.8 \text{ mJm}^{-2}$ in the current case. Above the upper limit, the stable state is not a skyrmion, but stripe domains as shown in Fig. 1e for $D = 5 \text{ mJm}^{-2}$. $E(R, w)$ of (8)

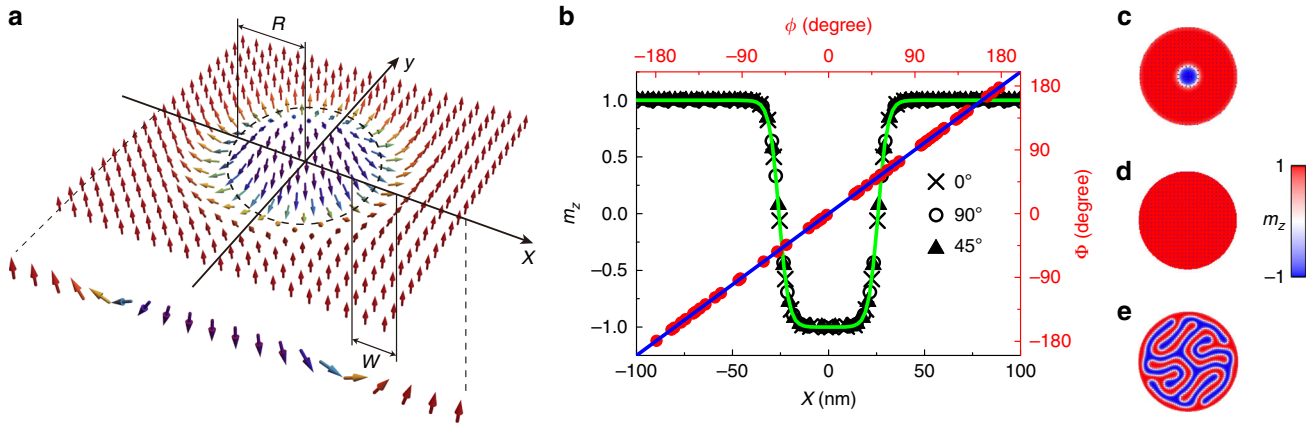


Fig. 1 Schematic diagram of an isolated skyrmion and its rotational symmetry. **a** Schematic diagram of a Néel skyrmion of radius R and wall (between the skyrmion core and the outer domain) width w in a 2D film. The arrows denote the spin direction. Spin orientations of the skyrmion along x axis are sketched below the main figure. **b** Right axis, ϕ -dependence of Φ (red circles); left axis, radial (r) distribution of $m_z = \cos\Theta$ along the diameters of $\phi = 0$ (crosses), 45° (triangles), and 90° (circles) for $A = 15 \text{ pJm}^{-1}$, $D = 3.7 \text{ mJm}^{-2}$, $K_u = 0.8 \text{ MJm}^{-3}$, and $B = 0$. The green solid line is the fit to $\Theta_{\text{dw}}(r) = 2 \arctan \left[\frac{\sinh(R/w)}{\sinh(r/w)} \right]$ with fitting parameters of $R = 25.77 \text{ nm}$ and $w = 4.94 \text{ nm}$. The blue solid line is $\Phi = \phi$. **c-e** Three typical equilibrium states obtained in the numerical simulations for different parameters. **c** Isolated skyrmion. **d** Single-domain state of $m_z = 1$ (or $m_z = -1$). **e** Stripe domains. The pixel color encodes the m_z component with the color bar shown in the figure

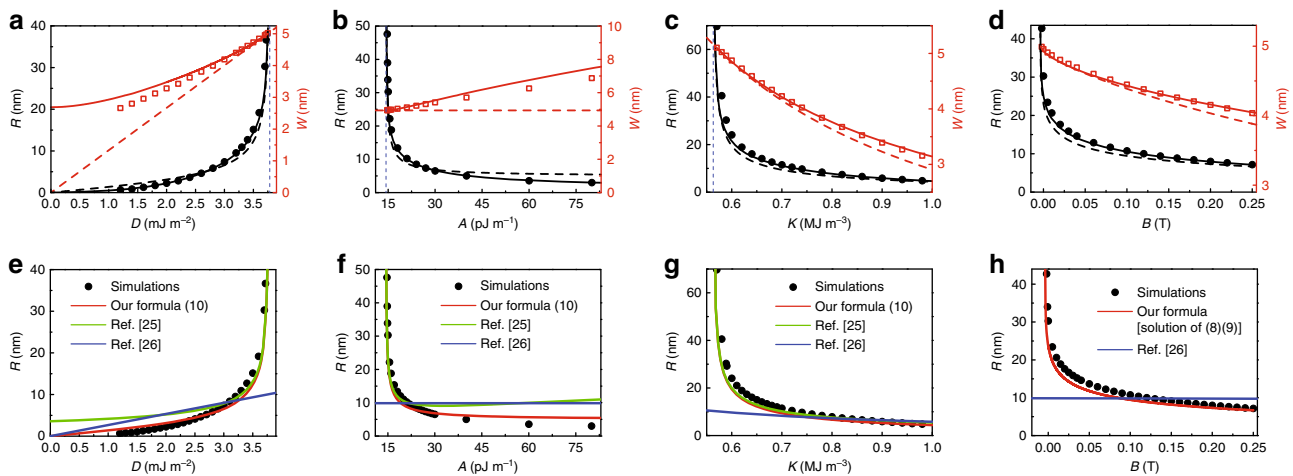


Fig. 2 Comparison between theoretical results and simulation results. The D (a), A (b), K (c), and B (d) dependence of the skyrmion size R (left axis) and wall width w (right axis). Model parameters are $A = 15 \text{ pJm}^{-1}$, $K = K_u - \mu_0 M_s^2/2 = 0.588 \text{ MJm}^{-3}$, $D = 3.7 \text{ mJm}^{-2}$, and $B = 0$. In each subfigure, one of these four parameters is treated as a tuning parameter and the other three parameters are fixed to above values. The symbols are the micromagnetic simulation data. The solid lines are exact analytic results obtained from Eq. (8). The dashed lines are approximate results of $R = \pi D \sqrt{\frac{A}{16AK^2 - \pi^2 D^2 K}}$, $w = \frac{\pi D}{4K}$ [subfigures a-c] and solution of Eqs (11) and (12) [subfigure (d)]. Vertical dashed lines are the upper (lower) bound of parameters above (below) which a stable skyrmion cannot exist. **e-h** The comparison of the skyrmion size R for the micromagnetic simulation (black dots), our formula Eq. (13) [or solution of Eqs (11) and (12) for non-zero B] (red lines), and previous studies ref. 25 (green lines), ref. 26 (blue lines)

has a minimum as long as $|D| < 3.8 \text{ mJm}^{-2}$ that indicates existence of the skyrmion. However, micromagnetic simulations show that the skyrmion can only exist in the window of $1.2 \text{ mJm}^{-2} < D < 3.8 \text{ mJm}^{-2}$ when the skyrmion size is larger than 1 nm in the current case. Below 1.2 mJm^{-2} , the stable state is a single domain with all spins pointing up or down as shown in Fig. 1d. This discrepancy may be due to the discretization of continuous LLG equation in micromagnetic simulations. In principle, the mesh size should be much smaller than the skyrmion size. For a skyrmion of 1 nm, our mesh size is 0.01 nm. Due to the limited precision of the MuMax3 package, the mesh size cannot be further decreased. There exists also a minimal A of around 14 pJm^{-1} as shown in Fig. 2b and a minimal K of around 0.56 MJm^{-3} as shown in Fig. 2c, below which the skyrmion does not exist, and the stable state is stripe domains as shown in Fig. 1e. The skyrmion size decreases with B , which is consistent with the experimental observations^{7,8,30}.

It is still unclear how R and w depend on A , D , and K although Eq. (8) agrees almost perfectly with the simulation results. Thus, it is highly desirable to have simple approximate expressions for R and w in terms of material parameters. The exchange and DMI energies come from the spatial magnetization variation rate. For a skyrmion, the magnetization variation rates in the radial and tangent directions scale respectively as $1/w$ and $1/R$. The exchange energy is then proportional to the skyrmion wall area of $\pi R w$ multiplying the square of the magnetization variation rates $1/R^2 + 1/w^2$, i.e., $E_{\text{ex}} \propto (R/w + w/R)$. The integrand of the second term (tangential term) of E_{DM} is proportional to $\sin 2\Theta$ due to the triple product of the interfacial DMI vector (along the radial direction), the tangential variation of \mathbf{m} (along the tangential direction), and \mathbf{m} itself. As $\sin 2\Theta$ is almost asymmetric about $r=R$ (positive when $r > R$ and negative when $r < R$) and is non-zero only near $r=R$, after integral over r , the second term in E_{DM} is vanishingly small. The DMI energy is then mainly contributed by the first term (radial term), which is proportional to wall area (Rw) multiplying the magnetization variation rate along radial direction ($1/w$), i.e., $E_{\text{DM}} \propto R$. The isotropic energy is mainly from the skyrmion wall area. Thus, $E_{\text{an}} \propto Rw$. The Zeeman energy of the skyrmion comes from the skyrmion core proportional to its area of $\pi(R - cw)^2$, where c is a coefficient depending on the magnetization profile and from the wall area proportional to its area of $\pi R w$. To obtain the proportional coefficients, one needs to find approximate expressions for $f_i(R/w)$ ($i = 1, \dots, 6$) in Eq. (8). In the case of $R \gg w$ (or $x \equiv R/w \gg 1$), $\sinh(x) \approx \cosh(x) \approx e^x$.

Thus, function $g(t, x) = [2 \sinh^2(x) \cosh^2(t)] / [\sinh^2(x) + \sinh^2(t)]^2 \approx 2e^{2(x-t)} / [e^{2(x-t)} + 1]$ is positive and significantly non-zero only near $t = x$, reflecting the fact that E_{ex} , E_{DM} , and E_{an} are mainly from the skyrmion wall region that is assumed to be very thin. Furthermore, the area bounded by $g(t, x)$ -curve and t -axis is 1 so that $g(t, x) \approx \delta(t - x)$ resembles the properties of a delta function. We can evaluate f_i 's under this approximation (see Methods and Supplementary Fig. 2). For example, $f_1(x)$ is

$$f_1(x) = \int_0^\infty g(t, x) t dt \approx \int_0^\infty \delta(x - t) t dt = x. \quad (9)$$

The total energy is then

$$E(R, w) = 4\pi d \left[A \left(\frac{R}{w} + \frac{w}{R} \right) - \frac{\pi}{2} DR + KwR + M_s B \left(\frac{R^2}{2} + \frac{\pi^2}{24} w^2 \right) \right]. \quad (10)$$

Due to the specific form of the magnetization profile of $\Theta_{\text{dw}}(r)$, Rw -term in E_{Ze} vanishes and $E_{\text{Ze}} \approx 4\pi M_s B \left(\frac{R^2}{2} + \frac{\pi^2}{24} w^2 \right)$. The skyrmion size and wall width are then the values that make $E(R,$

$w)$ minimal, or

$$A \left(\frac{1}{w} - \frac{w}{R^2} \right) - \frac{\pi}{2} D + Kw + M_s B R = 0, \quad (11)$$

$$A \left(-\frac{R}{w^2} + \frac{1}{R} \right) + KR + \frac{\pi^2}{12} M_s B w = 0. \quad (12)$$

For $B = 0$, Eqs. (11) and (12) can be analytically solved. The results are

$$R = \pi D \sqrt{\frac{A}{16AK^2 - \pi^2 D^2 K}}, \quad w = \frac{\pi D}{4K}. \quad (13)$$

The dashed lines in Fig. 2a–c are the approximate formulas that compare quite well with simulation results too. For $B \neq 0$, we do not have a closed-form solution of Eqs. (11) and (12) because they are a sextic equation for R or w (see Supplementary Note 2), but their numerical solutions are easily obtained that are plotted as dashed lines in Fig. 2d. In summary, our approximate formula agrees very well with the simulations for $R \gg w$ as expected from our approximation. For smaller skyrmions, the approximation is still not bad, and qualitatively gives correct parameter dependence. We can also determine the upper limit of D and lower limits of A , K , and B from the approximate formula. Since R must be real and finite, we have

$$16AK > \pi^2 D^2, \quad (14)$$

for $B = 0$, so that the upper limit of D and lower limits of A and K are obtained as $D < \frac{4}{\pi} \sqrt{AK}$, $A > \frac{\pi^2 D^2}{16K}$, and $K > \frac{\pi^2 D^2}{16A}$. The limit is also the critical value separating the uniform state from helical state³⁴. These critical values are plotted in Fig. 2a–c as vertical dashed lines that agrees also well with simulations.

Discussion

In our model, we took into account the shape anisotropy, but did not include the demagnetizing field due to the inhomogeneous part of the magnetization distribution. For very large and thin films, where the film thickness d is much smaller than R and w , the neglected demagnetizing field is vanishing small (see Supplementary Note 3 for a detailed proof). This is the case for those inversion-symmetry breaking systems with a single ferromagnetic layer, such as Pd/Fe/Ir^{8,30} and Pt/Co^{10,20}, but this approximation is not good for thick films with bulk DMI, such as MnSi¹⁹ and FeGe⁷, or those repeated multilayer systems¹². Since most device proposals are based on thin-film systems, our model has a wide applicability. For thick films, the magnetization is nonuniform in the third dimension, so that the skyrmion is no longer a two-dimensional (2D) magnetic texture. Twisted skyrmion tubes or bobbers may be energetically preferred³⁵. Our model as well as all the 2D theories at present is not applicable, and more complicated three-dimensional theories are needed for this case. For the exchange interaction, we only consider a nearest-neighbor exchange interaction characterized by a single parameter A . For those systems with significant exchange interactions beyond nearest neighbor^{36,37}, our model may not be directly applicable. However, if the extra exchange interaction (for instance, a next-nearest neighbor interaction) is small compared to A , its effect can be approximately considered by modifying A to an effective value A_{eff} ³⁸. Our model is a classical one, in which quantum fluctuations and finite-size effects are not considered. However, the comparison with ref. 30 (see Supplementary Fig. 3) shows that even for skyrmions as small as 1 nm, our model still gives good

results. The quantum fluctuations induce zero-point energy that helps stabilizing the skyrmions, and may be included in a phenomenological way by replacing the model parameters by effective ones³⁹. It is also worth mentioning that we consider the isolated skyrmions in infinite media. The edge confinement effect and skyrmion lattice are not the concern of this study.

We compare our theoretical results of the skyrmion size with the experimental results for Pd/Fe/Ir^{8,30,40} and W/Co₂₀Fe₆₀B₂₀/MgO^{10,41}, in which isolated skyrmions are observed. For Pd/Fe/Ir, the parameters are $M_s = 961 \sim 1160 \text{ kAm}^{-1}$, $A = 2 \sim 4.87 \text{ pJm}^{-1}$, $K = 2.5 \text{ MJm}^{-3}$, $D = 3.4 \sim 3.9 \text{ mJm}^{-2}$, and $B = 1.15 \sim 2.97 \text{ T}$ ^{8,30}. Our theory gives small skyrmion sizes of $0.53 \sim 1.59 \text{ nm}$ that compares well with the experimental results of $0.9 \sim 1.9 \text{ nm}$ in ref. ⁸. For W/Co₂₀Fe₆₀B₂₀/MgO, the parameters are $M_s = 650 \text{ kAm}^{-1}$, $A = 10 \text{ pJm}^{-1}$, $K = 0.02275 \text{ MJm}^{-3}$, $D = 0.68 \sim 0.73 \text{ mJm}^{-2}$, and $B = 0.00025 \sim 0.0005 \text{ T}$ ^{10,41}. Our theory gives large skyrmion sizes of $356 \sim 1484 \text{ nm}$, consistent with the experimental results of $700 \sim 2000 \text{ nm}$ in Ref. ¹⁰. Our theoretical results show good agreement with the experiments although some of the material parameters can only be roughly estimated from different publications. We also compare our analytic results with micromagnetic simulations for Pd/Fe/Ir^{8,30,40}, MnSi^{42,43}, and W/Co₂₀Fe₆₀B₂₀/MgO¹⁰. The skyrmion sizes range from several nanometers to about 2 micrometers. All the comparisons give quite good agreement (see Supplementary Figs. 3–5).

It is natural to extend our approach to Bloch skyrmions in the systems with bulk inversion symmetry broken. The bulk DMI energy $E_{\text{DM}} = D \iint \mathbf{m} \cdot (\nabla \times \mathbf{m}) dS$ can be rewritten as

$$E_{\text{DM}} = 2\pi D d \sin \gamma \int_0^\infty \left(\frac{d\Theta}{dr} + \frac{\sin 2\Theta}{2r} \right) r dr, \quad (15)$$

where $\gamma = \pm \pi/2$ gives minimal energy. Since all other discussions are the same as those for Néel skyrmions, the formulas of R and w are applicable to the Bloch skyrmions.

There are already a lot of studies on the size of skyrmions. In comparison with previous studies^{18,25–29}, our results show not only the correct behavior of the skyrmion size as a function of D , A , and K , but also the correct limit at $D = 0$. The correct result can be obtained only by treating R and w as independent variables. In Ref. ¹⁸, the skyrmion size in a skyrmion lattice with a spiral structure was found to be determined by D/A to some extent. This result is not true for an isolated skyrmion because the isolated skyrmion size depends sensitively on the anisotropy K ^{20,43} and the external magnetic field B ^{8,30}. Another well-cited formula is $R = \sqrt{\frac{A/K}{2[1-\pi D/(4\sqrt{A/K])}]}$ ²⁵. This formula gives correct critical condition for the existence of isolated skyrmions (Eq. (14)), and same critical behavior near the critical condition. However, the behavior at large A is incorrect: micromagnetic simulations show R always decreases with A , but according to this formula R increases with A at large A . Ref. ²⁶ gives another formula $R = \frac{D\pi^2}{2K\pi + 8M_s B/\pi}$ that does not depend on A . However, this behavior is inconsistent with simulations. There are also many other papers for the skyrmion size based on different ansatz about the skyrmion profile^{27,28,44}, but in those studies the skyrmion energy is assumed to be a function of the skyrmion size R only, while the skyrmion wall width w is either ignored or treated as a constant.

In contrast, we treated R and w as independent variables and obtained more satisfactory results. We compare micromagnetic simulation data against our approximate formula of the skyrmion size R (Eq. (13) or the numerical solution of Eqs. (11) and (12) (for $B \neq 0$), as well as the analytic formulars in refs. ^{25,26} in Fig. 2e–h to demonstrate the advance of our results. During the reviewing process of our paper, there are several new

studies on the same problem. In ref. ⁴⁵, similar approximate skyrmion energy in terms of R and w (Eq. (10)) was also obtained although two 180 domain walls were used instead of a 360° domain wall, the external magnetic field was not included, and no detailed derivation was given. In ref. ⁴⁶, similar approach was used and the magnetostatic energy due to both surface and volume magnetic charges was included. A bistability region in parameter space was found, in which two kinds of skyrmions with different sizes are predicted. The one with a larger size is stabilized mainly by demagnetizing field and the other is stabilized mainly by DMI (which is also discussed in ref. ⁴⁷). In our model, because of the ultra-thin film is assumed, the demagnetizing field is dominated by the the shape anisotropy of uniform magnetization, and the field due to the inhomogeneity of magnetization is vanishingly small. Thus, there is no bistable skyrmion structures that is also consistent with ref. ⁴⁶ and all our skyrmions are stabilized by DMI.

In conclusion, a single skyrmion can be well described by a 360° domain wall profile parametrized by two fundamental quantities, skyrmions size and wall width. Through the minimization of total energy with respect to the skyrmion size and wall width, we obtain analytic formulas for skyrmion size and wall width as a function of exchange stiffness, anisotropy coefficient, DMI strength, and external field. The formulas agree very well with simulations and experiments.

Methods

Numerical simulations. The numerical simulations are carried out by Mumax package. We consider a magnetic disk of diameter from 128 nm to 1024 nm and thickness 0.4 nm (see Supplementary Fig. 1). The mesh size of $1 \text{ nm} \times 1 \text{ nm} \times 0.4 \text{ nm}$ is used in our simulations for those skyrmions larger than 5 nm in radius. For skyrmions of $R < 5 \text{ nm}$, the mesh size is $0.1 \text{ nm} \times 0.1 \text{ nm} \times 0.4 \text{ nm}$. The skyrmion size R is obtained by finding the radius of the $m_z = 0$ contour line. The skyrmion wall width is obtained by fitting the simulated radial profile by the 360° domain wall profile with R obtained before.

Derivation of energy expressions. To derive the functions $f_i(x)$ in the energy expression, we substitute Eq. (7) into Eqs. (3)–(6). For the exchange energy, by defining $x = R/w$, $t = r/w$, we have

$$\begin{aligned} E_{\text{ex}} &= 2\pi A \int_0^\infty \left[\left(\frac{d\Theta}{dr} \right) + \frac{\sin^2 \Theta}{r^2} \right] r dr \\ &= 4\pi A \int_0^\infty \left\{ \frac{2 \sinh^2(x) \cosh^2(t)}{[\sinh^2(x) + \sinh^2(t)]^2} \right. \\ &\quad \left. + \frac{2 \sinh^2(x) \sinh^2(t)}{t[\sinh^2(x) + \sinh^2(t)]^2} \right\} dt \end{aligned}$$

Thus, we define

$$\begin{aligned} f_1(x) &= \int_0^\infty \frac{2 \sinh^2(x) \cosh^2(t)}{[\sinh^2(x) + \sinh^2(t)]^2} dt, \\ f_2(x) &= \int_0^\infty \frac{2 \sinh^2(x) \sinh^2(t)}{t[\sinh^2(x) + \sinh^2(t)]^2} dt. \end{aligned}$$

Although $R \gg w$ ($x \gg 1$), we have $\sinh(x) \approx \cosh(x) \approx e^x$, so that

$$f_1(x) \approx \int_0^\infty \frac{2e^{2(x-t)}}{[e^{2(x-t)} + 1]^2} t dt$$

The function $\frac{2e^{2(x-t)}}{[e^{2(x-t)} + 1]^2}$ is non-zero only for $x \approx t$. Approximately, we have

$$\frac{2e^{2(x-t)}}{[e^{2(x-t)} + 1]^2} \approx I_1 \delta(x - t),$$

where the coefficient I_1 is determined by

$$I_1 = \int_{-\infty}^\infty \frac{2e^{2x}}{(e^{2x} + 1)^2} dx = 1.$$

Thus, $f_1(x) \approx \int_0^\infty t \delta(x - t) dt = x$. Similarly, $f_2(x) \approx \int_0^\infty \delta(x - t)/t dt = 1/x$.

For the DM energy, we have

$$E_{\text{DM}} = 2\pi D \cos \gamma \int_0^\infty \left(\frac{d\theta}{dr} + \frac{\sin 2\theta}{2r} \right) r dr$$

$$= 4\pi D w \int_0^\infty \left[-\frac{\sinh x \cosh t}{\sinh^2 x + \sinh^2 t} t - \frac{\sinh x \sinh t (\sinh^2 x - \sinh^2 t)}{(\sinh^2 x + \sinh^2 t)^2} \right] dt.$$

We define

$$f_3(x) = -\int_0^\infty \frac{t \sinh x \cosh t}{\sinh^2 x + \sinh^2 t} dt,$$

$$f_4(x) = -\int_0^\infty \frac{\sinh x \sinh t (\sinh^2 x - \sinh^2 t)}{(\sinh^2 x + \sinh^2 t)^2} dt.$$

For $f_3(x)$, the function inside the integral $\frac{\sinh x \cosh t}{\sinh^2 x + \sinh^2 t} \approx \frac{e^{(x-t)}}{e^{2(x-t)}+1}$ is localized at $x = t$ so that we have the approximation

$$f_3(x) \approx -\int_0^\infty \frac{e^{(x-t)}}{e^{2(x-t)}+1} t dt$$

$$\approx -\int_0^\infty I_3 \delta(x-t) t dt$$

$$\approx I_3 x,$$

where I_3 is determined by $I_3 = \int_{-\infty}^\infty \frac{e^x}{e^{2x}+1} dx = \pi/2$. The integrand in f_4 is 0 at $r = 0$, $r = \infty$ and $r = R$. Furthermore, it has opposite signs for $r < R$ and $r > R$. So $f_4 \sim 0$ after the integration.

For the anisotropy energy, we have

$$f_5(x) = \int_0^\infty \frac{2t \sinh^2 x \sinh^2 t}{[\sinh^2 x + \sinh^2 t]^2} dt.$$

Similar to the exchange energy and DM energy, the anisotropy energy is only non-zero near $r = R$, too. The approximate form of function f_5 is the same as f_1 ,

$$f_5(x) \approx \int_0^\infty \frac{2t e^{2(x-t)}}{[e^{2(x-t)}+1]^2} dt$$

$$\approx \int_0^\infty t \delta(x-t) dt = x.$$

The Zeeman energy is non-zero for both the wall region and the skyrmion core. The function f_6 is

$$f_6(x) = \int_0^\infty \frac{\sinh^2 x}{\sinh^2 t + \sinh^2 x} t dt$$

Again, we replace sinh functions by exponential functions to obtain

$$f_6(x) \approx \int_0^\infty \frac{1}{e^{2(x-t)}+1} t dt$$

$$= -\frac{1}{4} \text{Li}_2(-e^{2x}),$$

where $\text{Li}_i(x)$ is the polylogarithm function defined by $\text{Li}_i(x) = \sum_{n=1}^\infty \frac{x^n}{n^i}$. The asymptotic form of $-\frac{1}{4} \text{Li}_2(-e^{2x})$ is

$$\lim_{x \rightarrow \infty} -\frac{1}{4} \text{Li}_2(-e^{2x}) = \frac{x^2}{2} + \frac{\pi^2}{24}$$

So we have $f_6(x) \approx \frac{x^2}{2} + \frac{\pi^2}{24}$. The functions $f_1 \sim f_6$ as well as their approximate forms are plotted in Supplementary Fig. 2.

Data availability. The data that support the plots within this paper and other findings of this study are available from the corresponding author on reasonable request.

Received: 30 January 2018 Accepted: 30 May 2018

Published online: 04 July 2018

References

1. Skyrme, T. H. R. A unified field theory of mesons and baryons. *Nuclear Phys.* **31**, 556–569 (1962).
2. Rößler, U. K., Bogdanov, A. N. & Pfleiderer, C. Spontaneous skyrmion ground states in magnetic metals. *Nature* **442**, 797–801 (2006).
3. Mühlbauer, S. et al. Skyrmion lattice in a chiral magnet. *Science* **323**, 915–919 (2009).
4. Yu, X. Z. et al. Real-space observation of a two-dimensional skyrmion crystal. *Nature* **465**, 901–904 (2010).
5. Onose, Y., Okamura, Y., Seki, S., Ishiwata, S. & Tokura, Y. Observation of magnetic excitations of skyrmion crystal in a helimagnetic insulator Cu_2OSeO_3 . *Phys. Rev. Lett.* **109**, 037603 (2012).
6. Park, H. S. et al. Observation of the magnetic flux and three-dimensional structure of skyrmion lattices by electron holography. *Nat. Nanotechnol.* **9**, 337–342 (2014).
7. Du, H. et al. Edge-mediated skyrmion chain and its collective dynamics in a confined geometry. *Nat. Commun.* **6**, 8504 (2015).
8. Romming, N. et al. Writing and deleting single magnetic skyrmions. *Science* **341**, 636–639 (2013).
9. Heinze, S. et al. Spontaneous atomic-scale Magnetic skyrmion lattice in two dimensions. *Nat. Phys.* **7**, 713–718 (2011).
10. Jiang, W. et al. Blowing magnetic skyrmion bubbles. *Science* **349**, 283–286 (2015).
11. Krause, S. & Wiesendanger, R. Spintronics: Skyrmionics gets hot. *Nat. Mater.* **15**, 493–494 (2016).
12. Woo, S. et al. Observation of room-temperature magnetic skyrmions and their current-driven dynamics in ultrathin metallic ferromagnets. *Nat. Mater.* **15**, 501–506 (2016).
13. Li, J. et al. Tailoring the topology of an artificial magnetic skyrmion. *Nat. Commun.* **5**, 4704 (2014).
14. Boeck, A. H. & Torre, E. Della *Magnetic Bubbles*. (North-Holland, Amsterdam, 1975).
15. Malozemoff, A. P. and Slonczewski, J. C. *Magnetic Domain Walls in Bubble Materials* (Academic Press, New York, United States, 1979).
16. Thiele, A. A. Theory of the static stability of cylindrical domains in uniaxial platelets. *J. Appl. Phys.* **41**, 1139 (1970).
17. Thiaville, A. & Pátek, K. Conical bubbles. *J. Magn. Magn. Mater.* **124**, 355–367 (1993).
18. Iwasaki, J., Mochizuki, M. & Nagaosa, N. Universal current-velocity relation of skyrmion motion in chiral magnets. *Nat. Commun.* **4**, 1463 (2013).
19. Nagaosa, N. & Tokura, Y. Topological properties and dynamics of magnetic skyrmions. *Nat. Nanotech.* **8**, 899–911 (2013).
20. Sampaio, J., Cros, V., Rohart, S., Thiaville, A. & Fert, A. Nucleation, stability and current-induced motion of isolated magnetic skyrmions in nanostructures. *Nat. Nanotechnol.* **8**, 839–844 (2013).
21. Zhou, Y. & Ezawa, M. A. Reversible conversion between a skyrmion and a domain-wall pair in a junction geometry. *Nat. Commun.* **5**, 4652 (2014).
22. Dürrenfeld, P., Xu, Y., Åkerman, J. & Zhou, Y. Controlled skyrmion nucleation in extended magnetic layers using a nanocontact geometry. *Phys. Rev. B* **96**, 054430 (2017).
23. Kong, L. & Zang, J. Dynamics of an insulating Skyrmion under a temperature gradient. *Phys. Rev. Lett.* **111**, 067203 (2013).
24. Yuan, H. Y. & Wang, X. R. Skyrmion creation and manipulation by nano-second current pulses. *Sci. Rep.* **6**, 22638 (2016).
25. Rohart, S. & Thiaville, A. Skyrmion confinement in ultrathin film nanostructures in the presence of Dzyaloshinskii-Moriya interaction. *Phys. Rev. B* **88**, 184422 (2013).
26. Zhang, X., Zhou, Y., Ezawa, M., Zhao, G. P. & Zhao, W. Magnetic skyrmion transistor: skyrmion motion in a voltage-gated nanotrack. *Sci. Rep.* **5**, 11369 (2015).
27. Castro, M. A. & Allende, S. Skyrmion core size dependence as a function of the perpendicular anisotropy and radius in magnetic nanodots. *J. Magn. Magn. Mater.* **417**, 344–348 (2016).
28. Vidal-Silva, N., Riveros, A. & Escrig, J. Stability of Néel skyrmions in ultrathin nanodots considering Dzyaloshinskii-Moriya and dipolar interactions. *J. Magn. Magn. Mater.* **443**, 116–123 (2017).
29. Lenov, A. O. et al. The properties of isolated chiral skyrmions in thin magnetic films. *New J. Phys.* **18**, 065003 (2016).
30. Romming, N., Kubetzka, A., Hanneken, C., von Bergmann, K. & Wiesendanger, R. Field-dependent size and shape of single magnetic skyrmions. *Phys. Rev. Lett.* **114**, 177203 (2015).
31. Braun, H.-B. Fluctuations and instabilities of ferromagnetic domain-wall pairs in an external magnetic field. *Phys. Rev. B* **50**, 16485 (1994).
32. Siemans, A., Zhang, Y., Hagemester, J., Vedmedenko, E. Y. & Wiesendanger, R. Minimal radius of magnetic skyrmions: statics and dynamics. *New J. Phys.* **18**, 045021 (2016).
33. Vansteenkiste, A. et al. The design and verification of MuMax3. *AIP Adv.* **4**, 107133 (2014).
34. Dzyaloshinskii, I. E. The Theory of helicoidal structures in antiferromagnets. II. Metals. *Zh. Eksp. Teor. Fiz.* **47**, 992 (1964). [*Sov. Phys. JETP* **20**, 665 (1965)].
35. Zheng, F. et al. Experimental observation of chiral magnetic bobbles in B20-type FeGe. *Nat. Nanotechnol.* **13**, 451–455 (2018).
36. Dupé, B., Hoffmann, M., Paillard, C. & Heinze, S. Tailoring magnetic skyrmions in ultra-thin transition metal film. *Nat. Commun.* **5**, 4030 (2014).
37. Leonov, A. O. & Mostovoy, M. Multiply periodic states and isolated skyrmions in an anisotropic frustrated magnet. *Nat. Commun.* **6**, 9275 (2015).

38. Yuan, H. Y., Gomonay, O. & Kläui, M. Skyrmions and multisublattice helical states in a frustrated chiral magnet. *Phys. Rev. B* **96**, 134415 (2017).
39. Keesman, R. et al. Degeneracies and fluctuations of Néel skyrmions in confined geometries. *Phys. Rev. B* **92**, 134405 (2015).
40. Simon, E., Palotás, K., Rózsa, L., Udvardi, L. & Szunyogh, L. Formation of magnetic skyrmions with tunable properties in PdFe bilayer deposited on Ir (111). *Phys. Rev. B* **90**, 094410 (2014).
41. Jaiswal, S. et al. Investigation of the Dzyaloshinskii-Moriya interaction and room temperature skyrmions in W/CoFeB/MgO thin films and microwires. *Appl. Phys. Lett.* **111**, 022409 (2017).
42. Karhu, E. A. et al. Chiral modulations and reorientation effects in MnSi thin films. *Phys. Rev. B* **85**, 094429 (2012).
43. Wilson, M. N., Butenko, A. B., Bogdanov, A. N. & Monchesky, T. L. Chiral skyrmions in cubic helimagnet films: the role of uniaxial anisotropy. *Phys. Rev. B* **89**, 094411 (2014).
44. Tomasello, R. et al. Origin of temperature and field dependence of magnetic skyrmion size in ultrathin nanodots. *Phys. Rev. B* **97**, 060402 (2018).
45. Kravchuk, V. P., Sheka, D. D., Rößler, van den Brink, U. K. J. & Gaididei, Y. *Phys. Rev. B* **97**, 064403 (2018).
46. Büttner, F., Lemesch, I. & Beach, G. S. D. Theory of isolated magnetic skyrmions: from fundamentals to room temperature applications. *Sci. Rep.* **8**, 4464 (2018).
47. Bernand-Mantel, A. et al. The skyrmion-bubble transition in a ferromagnetic thin film. Preprint at <https://arxiv.org/abs/1712.03154> (2017).

Acknowledgements

This work was supported by the National Natural Science Foundation of China (Grant Numbers 11774296 and 61704071), as well as Hong Kong RGC Grants Numbers 16300117 and 16301816. X.S.W. acknowledge support from UESTC and China Post-doctoral Science Foundation (Grant Number 2017M612932).

Author contributions

X.S.W. carried out the theoretical calculations and the numerical simulations. H.Y.Y. discussed the results. X.S.W. and X.R.W. wrote the manuscript with input from H.Y.Y.

Additional information

Supplementary Information accompanies this paper at <https://doi.org/10.1038/s42005-018-0029-0>.

Competing interests: The authors declare no competing interests.

Reprints and permission information is available online at <http://npg.nature.com/reprintsandpermissions/>

Publisher's note: Springer Nature remains neutral with regard to jurisdictional claims in published maps and institutional affiliations.



Open Access This article is licensed under a Creative Commons Attribution 4.0 International License, which permits use, sharing, adaptation, distribution and reproduction in any medium or format, as long as you give appropriate credit to the original author(s) and the source, provide a link to the Creative Commons license, and indicate if changes were made. The images or other third party material in this article are included in the article's Creative Commons license, unless indicated otherwise in a credit line to the material. If material is not included in the article's Creative Commons license and your intended use is not permitted by statutory regulation or exceeds the permitted use, you will need to obtain permission directly from the copyright holder. To view a copy of this license, visit <http://creativecommons.org/licenses/by/4.0/>.

© The Author(s) 2018